

1 Focal mechanisms of small earthquakes beneath the
2 Japanese islands based on first-motion polarities picked
3 using deep learning

4 Takahiko Uchide^{1,*}

5 ¹ Geological Survey of Japan, National Institute of Advanced Industrial Science and
6 Technology (AIST)

7 Abbreviated Title: Focal Mechanisms in the entire Japanese islands

8 * Corresponding Author: Takahiko Uchide (t.uchide@aist.go.jp)

9 Summary

10 Knowledge of crustal stress fields is essential for understanding tectonics and
11 earthquake generation. One approach for estimating the crustal stress field is based on
12 the focal mechanisms of earthquakes. This study investigated the focal mechanisms of
13 approximately 110,000 microearthquakes in the area of the Japanese islands that
14 occurred at a depth shallower than 20 km, based on the first-motion polarities picked by
15 a simple neural network model. The model was first trained using a data set of mainly
16 moderate to large earthquakes throughout Japan. Following on, the model was
17 re-trained using a data set of microearthquakes in two regions of Japan. The threshold of
18 the confidence score from the neural network model was chosen to maximize the
19 overall quality of the focal mechanism solutions. The P- and T-axes of the numerous
20 focal mechanism solutions provided more detailed distributions of the crustal stress
21 field. For example, in the Chugoku region, small differences were observed in the trend
22 of P-axes azimuths between the northern and southern areas, spatially corresponding to
23 geodetic observations. The results of this study are useful for revealing the crustal stress
24 field, and, as such, for assessing past and current tectonic activities and potential future
25 earthquake generation.

26 Keywords

- 27 ● Earthquake source observations
- 28 ● Seismicity and tectonics
- 29 ● Neural networks, fuzzy logic

1. Introduction

Crustal stress field data is crucial for understanding tectonics and seismic activity; however, measuring the stress at depths over a large area is challenging. Direct measurements at specific boreholes (e.g., Wu *et al.* 2007; Huffman *et al.* 2016; Brodsky *et al.* 2017; Townend *et al.* 2017) offer detailed information but only as it concerns one spot. In contrast, seismology provides indirect measurements for a wider area but includes more uncertainty. The focal mechanisms, which indicate the fault plane and slip directions, specify the orientation of seismogenic stress. The World Stress Map (Heidbach *et al.* 2008; Heidbach *et al.* 2016; Heidbach *et al.* 2018) presents the global compilation of this information.

In the past, routinely determined moment tensor solutions were used for estimating regional stress fields (Terakawa and Matsu'ura 2010; Hardebeck 2015). However, non-estimated areas remain, even in seismically active areas such as the Japanese islands. More complete knowledge of the seismogenic stress field requires focal mechanisms for microearthquakes, particularly in low seismicity areas (e.g., Imanishi *et al.* 2011; Imanishi *et al.* 2012; Matsumoto *et al.* 2015). Comprehensive investigations of microearthquake focal mechanisms contributed to revealing the regional stress field (e.g., Iio *et al.* 2018; Imanishi *et al.* 2019).

The focal mechanisms of moderate or larger earthquakes can be automatically determined using the full waveform from the local (e.g., Dreger and Helmberger 1993; Fukuyama *et al.* 1998) or global (e.g., Ekström *et al.* 2012) seismic network. However, the mechanisms of small earthquakes cannot be similarly determined due to the difficulty of modeling high-frequency seismograms. Instead, the first-motion polarity is

typically used in this regard, where the vertical component initially moves either upward or downward. Automatic polarity-picking methods include an approach based on the sign of the first extremum after the P arrival (Nakamura 2004; Chen and Holland 2016). Pugh et al. (2016a) proposed a Bayesian approach using the first extremum and a probability function of P arrival time. Recently, deep learning allowed for automatically picking the polarity (Ross *et al.* 2018; Hara *et al.* 2019). Deep learning has the approximation capabilities of a multilayer neural network to arbitrary functions (Hornik 1991). This presents an advantage in the polarity-picking problem, which involves the polarity of the first pulse and the various forms of seismic noise.

This study aimed to obtain focal mechanism solutions for the Japanese islands, one of the most seismically active regions in the world. The first-motion polarities were picked using a neural network model and seismic data from nationwide seismic networks. Finally, the focal mechanism solutions and spatial trends in P- and T-axes were reviewed.

2. Training the Neural Network Model

2.1. Design of the Neural Network Model

Fig. 1 summarizes the neural network used in this study. The input of the neural network model was a 256-sample-long seismogram in which the 156th sample corresponded to the P-arrival time already picked either manually or automatically. The output comprised two scores (confidence scores) corresponding to the upward and downward polarities. Note that, in the case of Southern California, Ross et al. (2018) classified the polarity as “up,” “down,” and “unknown”; however, in this study, the

“unknown” class was not set. The data set included many seismograms with impulsive onset but no polarity information (Fig. 2), and the lack of polarity information did not indicate “unknown” in this case. Thus, no training data set was available for the “unknown” class and such a class could not be set for the present study. In the cases with first-motion polarities being ambiguous, the confidence scores for both polarities are expected to have similar values. A confidence threshold was set for this research at a subsequent stage to accept suggested polarity information for determining the focal mechanism.

A simple neural network model (Fig. 1) similar to those used in prior studies (Ross *et al.* 2018; Hara *et al.* 2019) was designed. The neural network model started with two convolution layers, followed by three units comprising convolution, batch normalization (Ioffe and Szegedy 2015), and the maximum pooling layers. The model ended with two fully connected layers. The kernel size of the convolutional layers was 11. For all but the final layers, the activation function was the rectified linear units (known as “ReLU”) (Nair and Hinton 2010); the SoftMax function was chosen for the final layer:

$$\text{softmax}(\mathbf{z})_i = \frac{\exp(z_i)}{\sum_j \exp(z_j)}, \quad (1)$$

where $\mathbf{z} = (z_1, z_2)$ is the output of the final layer corresponding to the upward and downward polarities, respectively. The final outputs (confidence scores) are non-negative and their summation is always 1.

2.2. Training Procedure

Generally, the training of neural network models requires training, validation, and test data sets. In this study, the data sets comprised the seismograms and the polarity. The

training data set was used for optimizing the parameters in the neural network model. The initial values of the model parameters were randomly set. The negative log-likelihood function was employed as a loss function to quantify the difference between the output of the model and the polarity expectation from the training data set, i.e., (1, 0) for the upward polarity and (0, 1) for the downward polarity. The value of the loss function was simply called a loss. The parameters of the neural network model were updated by back-propagating the loss (Rumelhart et al. 1986) optimized by the adaptive moment estimation (known as “Adam”) method (Kingma and Ba 2014). This optimization was iteratively performed to decrease the loss.

The problem to be carefully addressed is the overfitting problem that the trained model works well with the training data but poorly with unseen data. This study addressed the overfitting problem in two ways. One was by using the dropout technique (Srivastava et al. 2014), where 50% of randomly selected perceptions were muted during the training. The second approach involved performing cross-validation using a validation data set that was independent of the training set. If the loss for the validation data set increased as the training progressed, while that for the training data set decreased for 10 iterations (epochs), the training was stopped.

Following the completion of the training, the performance of the trained model was examined using another data set (test data set) of small to microearthquakes, as the present study focused on such small events.

Since the data set of microearthquakes available in this study was small, training of the neural network model was performed in two stages. In the first stage, training was carried out using a large data set of moderate to large earthquakes to learn the

polarity-picking problem in general. The second stage employed microearthquake data for re-training the model. This reflected a fine-tuning approach (Girshick et al. 2014) during which all the parameters were optimized in both stages. The merit of this two-stage approach will be illustrated later by the results of the training.

2.3. Data

In the first stage, the Hi-net and the Japan Meteorological Agency (JMA) data of 19,341 earthquakes with P arrival and polarity data in the JMA catalog were used. Most of these earthquakes were larger than M 3 (Fig. 3). All the data were then spatially divided into the training and validation data sets (Fig. 4a; Table 1). Here, we should care the data leakage problem that the validation data set includes similar or identical data to one included in the training data set and cannot properly detect the overfitting problem. The spatial division of the data set was adopted in order to reduce the risk that similar data from collocated events at the same stations are included both in the training and validation data sets.

In the second stage, the model was trained using the P arrival time and polarity of microearthquakes in the Kanto and Chugoku regions, which were manually picked by Geological Survey of Japan, National Institute of Advanced Industrial Science and Technology (AIST). The Kanto data was also used by Imanishi et al. (2019). The majority of earthquakes in these data sets were smaller than M 3 (Fig. 3). The magnitude–frequency distributions were similar to that of the target data set (see Section 3), which will be introduced later. The spatial distributions of events in the Kanto and Chugoku regions are shown in Figs. 4b and 4c, respectively. The number of seismogram sets and earthquakes is summarized in Table 1.

In both stages, seismograms of the vertical component were used. The seismograms had 256 samples, i.e., 156 samples before and 100 samples after P arrival. The samples were 2.56 s long, as the data was sampled at 100 Hz. Low-frequency noise was removed by applying a high-pass filter at 1 Hz. The initial portion of the P-wave was emphasized by clipping seismograms at a particular threshold. Finally, each seismogram was normalized by its maximum value. Seismograms with amplitudes larger than the clipping threshold were normalized by the clipping threshold.

Furthermore, the data was augmented four times by flipping the seismograms upside down and by using time-shifting. The flipping procedure equalized the number of upward and downward polarity data. The time shift addressed the potential misalignment of data due to uncertainties in the arrival-time picking. Various values of the clipping threshold and the time-shift range were subsequently examined.

2.4. Results

A hundred cases with randomly selected clipping thresholds in the range of 10^{-6} to 10^{-4} m/s and with the half-width of the time-shift ranging 0–30 samples were examined. Note that, since the amplitudes of most of the seismograms were smaller than 10^{-4} m/s, in the case of such a large clipping threshold, seismograms were not clipped and were simply normalized by their maximum values. The results were evaluated based on the loss value for the test data set. The results indicated that the shorter the half-width of the time-shift range, the smaller the loss (Fig. 5a). The clipping threshold did not correlate with the loss value (Fig. 5b).

Hereafter, time-shift was not applied and 10^{-5} m/s was used as the clipping threshold. The neural network model was trained using these values.

The performance of the trained neural network model was quantified based on precision and recall. The precision represented how reliable the model prediction was. By focusing on one of the classes (upward or downward), the precision is defined as:

$$\text{Precision} = \frac{\text{TP}}{\text{TP} + \text{FP}}, \quad (2)$$

where TP represents a true positive, where the neural network model correctly predicts the designated class, and FP is a fault positive, where the model incorrectly predicts the designated class. Thus, TP and FP for the upward and downward polarities are:

$$\begin{aligned} \text{TP}_{\text{up}} &= N_{\text{uu}}, & \text{FP}_{\text{up}} &= N_{\text{du}}, \\ \text{TP}_{\text{down}} &= N_{\text{dd}}, & \text{FP}_{\text{down}} &= N_{\text{ud}}, \end{aligned} \quad (3)$$

where N_{ij} is of class i and predicted as class j , and “u” and “d” indicate the upward and downward polarities, respectively. Here, this study acknowledges that the model predicted the upward and downward polarity only when the confidence scores were larger than the confidence threshold. Otherwise, the model prediction is considered to have been ambiguous.

The recall represents how much data of the designated class is recovered by the neural network model, and is defined as:

$$\text{Recall} = \frac{\text{TP}}{\text{TP} + \text{FN}}, \quad (4)$$

where FN is a false negative, where the model incorrectly predicts the designated class, and

$$\text{FN}_{\text{up}} = N_{\text{ud}} + N_{\text{ua}}, \quad \text{FN}_{\text{down}} = N_{\text{du}} + N_{\text{da}}, \quad (5)$$

where the subscript “a” indicates ambiguous, where the confidence score is lower than the confidence threshold.

As the precision and the recall are functions of the confidence threshold, a curve of precision and recall can be drawn as shown in Fig. 5c. The better the model performance, the closer to the top right corner the precision-recall curve will be. Comparing the curves for the model trained only by the JMA data set and for the model trained also by the microearthquake data set, the latter showed observably better results. The performances of the models for upward and downward polarities were almost the same.

3. Application to Crustal Earthquakes in Japan

This study applied the trained model to the target data that is event data of earthquakes that occurred in the period 2005–2019 at depths of less than 20 km within the coastline in Japan islands, excluding the events for which polarity information was already available in the JMA catalog (Table 1). The study employed 2,301,584 seismogram sets of 114,525 events from Hi-net and the JMA seismic network, with P-wave arrival times taken from the JMA catalog. The magnitude–frequency distribution of earthquakes analyzed is shown in Fig. 3. Preprocessing was done in the same manner as in the model training. Good results were obtained for polarity picking with high confidence scores (Fig. 6), even in noisy cases.

The focal mechanisms were determined using polarity information with confidence scores larger than a confidence threshold and the HASH code (Hardebeck and Shearer 2002, 2008). The quality of focal mechanisms depended on the confidence threshold (Fig. 5d). If the threshold was too high, the very small number of polarity picks could not properly constrain focal mechanisms. If the threshold was lower than 0.7, the

fraction of A and B ranks given by the HASH code (Hardebeck and Shearer 2008) was almost constant. This study adopted a confidence threshold of 0.7 and, accordingly, 1,800,937 polarity picks were used.

Fig. 7 shows the estimated focal mechanisms and their P- and T-axes, in addition to the NIED F-net moment tensor solutions for reference. The focal mechanisms of 114,525 events were estimated, while those of 5,715 events were undetermined because the number of seismic stations was smaller than eight. Ranks A, B, C, and D, given by the HASH code (Hardebeck and Shearer 2008), were assigned to 1,582, 22,604, 43,486, and 41,138 events, respectively. The focal mechanism solutions covered much more space than those in a routine catalog.

4. Discussion

4.1. Quality of the First-motion Polarity Picking and Focal Mechanism Solutions

Somewhat surprisingly, the narrower the time-shift range of the data, the better the model performed (Fig. 5a). This was because the time-shifting made the model more flexible and robust to uncertainties in arrival-time picking. There were two potential reasons for this; one was that the arrival times in the test data were accurate because of careful review by an analyst, and, accordingly, the time-shift was not required. Another possible reason was that the training was not sufficient due to the shortage of microearthquake training data.

The stability of the performance of the trained model was measured by, in addition to the test data set, a comparison of the confidence scores for similar seismic data. First, using a repeating earthquake catalog (Igarashi 2020), 1,673 repeating earthquake pairs

were taken. For each event pair, seismogram pairs from identical stations were included. In total, 26,228 pairs of seismograms were selected. Next, the confidence scores of the pairs were compared using the product of the modified confidence scores as a measure of similarity, where the modified confidence score was confidence score of the downward polarity subtracted from that of the upward polarity, to establish their range from -1 to 1 . The histogram of the products is shown in Fig. 8. Most of the products were close to 1 , which meant a high similarity for the outcome of the trained model. Some cases were close to -1 . Examples of the seismograms in such cases are shown in Fig. 9, where some had noticeable opposite polarities, while others may have been affected by noise. This investigation suggested that the model worked well in most cases, although room for improvement remains.

Determination of focal mechanisms from the first-motion polarities of P-waves picked by the trained neural network model was also important for assessing the quality of polarity picking. In this study, 40.9% of the focal mechanism solutions were ranked D or “undetermined”. In a study on the determination of the focal mechanisms of earthquakes in Southern California using manually picked P-wave polarity and the amplitude ratio of P and S waves (Yang et al. 2012), the results showed that 56.6% (101,309 among 178,899) of events were ranked D, comparable to the result of the present study. Thus, the present study yielded a reasonable quality of P-wave first-motion polarity picking; however, based on several factors, this comparison is not entirely straightforward. These factors include differences in observational conditions such as the magnitude range and station density. Focal mechanism determination can be improved in several ways, e.g., by the introduction of P-wave amplitude (e.g.,

Matsushita and Imanishi 2015; Pugh *et al.* 2016b) and the ratio of P- and S-wave amplitudes (Hardebeck and Shearer 2003; Yang *et al.* 2012), alongside the application of advances in P-wave polarity picking.

The quality of the focal mechanism solutions is shown by region in Fig. 5e. In particular, the quality in the Hokkaido region was much worse than in other regions. The reason for this was examined by focusing on the number of stations. First, the quality of the focal mechanism solutions showed a good correlation with the number of stations (Fig. 5f). Next, the number of usable stations was smaller in Hokkaido than in other regions. This was likely because of the spatial density of seismic stations (Fig. 7e). Hence, it was more difficult to determine the focal mechanisms in Hokkaido than elsewhere.

4.2. Implications for the Stress Field

The spatial distribution of the P- and T-axis azimuths (Figs. 7c and 7d) suggested the placement of crustal stress field in the Japanese islands. In this regard, first the consistency of this study using the F-net catalog on a large scale is confirmed, before briefly discussing the advantages of this study, particularly at small spatiotemporal scales.

The overall features in the spatial distributions of the P- and T-axis azimuths from this study and the F-net catalog were similar. Note that the events investigated by this study and those included in the F-net catalog were largely different, as implied by the different magnitude distributions (Fig. 3). Accordingly, an overview of the spatial trend is provided by introducing two parameters from directional statistics, i.e., mean direction and circular standard deviation (CSD) (e.g., Ley and Verdebout 2017). The

mean direction of directional data $(\theta_1, \theta_2, \dots, \theta_N)$ is defined as $\bar{\theta}$, which satisfies the following equations:

$$\cos \bar{\theta} = \bar{C} = \frac{1}{N} \sum_{i=1}^N \cos \theta_i, \quad \sin \bar{\theta} = \bar{S} = \frac{1}{N} \sum_{i=1}^N \sin \theta_i. \quad (6)$$

The CSD, V , in the radian is defined as:

$$V = (-2 \ln \bar{R})^{1/2} \quad (7)$$

where the mean resultant length, \bar{R} , is:

$$\bar{R} = \sqrt{\bar{C}^2 + \bar{S}^2} \quad (8)$$

The mean directions of P- and T-axis azimuths from this study and the F-net catalog at 0.5-degree grids are shown in Fig. 10. The differences in the mean directions from this study and those in the F-net catalog were $\sim 7^\circ$ – 8° , which were within the CSD ($\sim 24^\circ$) of the present study and thus not significant. No spatial trends were observed in the differences. Interestingly, the CSD of the P- and T-axes mean directions were systematically larger in the northeast Japan than in the southwest Japan. This was likely because of actual variation in the axes, rather than uncertainty in the focal mechanism determination because the qualities of the focal mechanism solutions did not include such a trend (Fig. 5e).

In the Chugoku region, the P-axes struck in the east–west direction in the northern area (San-in area), whereas those that struck in the northwest–southeast direction did so in the southern area (Sanyo area). The contrast between P-axes azimuths in western Tottori was reported by Kawanishi et al. (2009). The present study also indicated a similar trend for the entire Chugoku region. This contrast geographically corresponded to the San-in shear zone (Meneses-Gutierrez and Nishimura 2020). A combination of

the current study alongside geodetic implications will further help to enhance an understanding of seismotectonics.

Local abnormal stress fields can be detected by focal mechanisms. In the Kansai region (Fig. 11), the majority of earthquakes exhibited east–west striking P-axes and north–south T-axes, while groups of events with different trends were also observed, i.e., one group of normal faulting events with P-axes in the north–south direction, and another group of events with northeast–southwest P-axes and northwest–southeast T-axes. Knowing the origins of such local stresses will be helpful to tectonic studies.

Rich focal mechanism data will also assist the study of temporal changes in the stress field. Fig. 12 shows the orientations of the T-axes before and after the 2016 Kumamoto earthquake in central Kyushu. T-axes tend to be in the north–south direction, as indicated by existing studies (e.g., Matsumoto *et al.* 2015; Savage *et al.* 2016). Small changes in the T-axes azimuths at the 2016 Kumamoto earthquake may have been due to, e.g., the stress rotation effected by large foreshocks and the mainshock (Yoshida *et al.* 2016), or as a result of different fault geometries. Additional investigation is needed in this regard.

Following the 2011 Tohoku-oki earthquake, several events occurred with T-axes in the east–west direction along the Pacific coast of the Kanto and Tohoku regions, whereas the majority of events in the entire Kanto and Tohoku regions had P-axes in this direction. This seismicity was activated following the 2011 Tohoku-oki earthquake. The focal mechanisms of microearthquakes prior to the 2011 Tohoku-oki earthquake were similar to those following the same earthquake in the northern Ibaraki prefecture, the Fukushima Hamadori area (Imanishi *et al.* 2012; Otsubo *et al.* 2018), and the

Kitakami mountain range (Yoshida et al. 2015). In the present study, the small number of focal mechanisms in the Boso peninsula before the Tohoku-oki earthquake were similar to those after this earthquake (Fig. 13). The east–west extensional stress field in these areas may have existed before the 2011 Tohoku-oki earthquake.

Despite the dramatic increase in focal mechanism solutions, there remain unstudied areas among the Japanese islands, where seismicity is relatively low. Accordingly, this type of study may be required for even smaller earthquakes, a more complex challenge than that addressed in the present study. Additional campaign seismic observations may improve the focal mechanism solutions for very small earthquakes. Furthermore, combining these observations with research that includes geological, geographical, and geodetical observations will improve our understanding of the crustal stress field and its origin.

5. Conclusions

In this study, the focal mechanisms of small to microearthquakes were estimated for gaining a better understanding of the crustal stress fields in the area of the Japanese islands. The focal mechanisms were derived using P-wave first-motion polarities, picked by a neural network model that takes the vertical component of seismograms with P arrival times as input. The focal mechanisms of almost all microearthquakes in the entire area of the Japanese islands were successfully determined. The focal mechanism solutions were generally consistent with the stress regime on a large scale. For example, the slight but observable differences in the P-axis azimuths in the northern and southern parts of the Chugoku region were consistent with the geodetic

observations for this region. The results of this study will be useful for revealing the crustal stress field, and, accordingly, for assessing past and current tectonic activities and future earthquake generation.

Acknowledgements

I thank Kazutoshi Imanishi and Reiken Matsushita for providing phase data for microearthquakes in Kanto and Chugoku regions in Japan. I also thank the NIED, especially Takanori Matsuzawa, for helping me prepare the large seismic data set. Careful reviews and constructive comments by the Editor Eiichi Fukuyama and two anonymous reviewers improved this paper. I used seismic data from NIED Hi-net (National Research Institute for Earth Science and Disaster Resilience 2020) and JMA available at <https://www.hinet.bosai.go.jp/?LANG=en> (last accessed on 19 August 2020), the phase data from the JMA Unified Earthquake Catalog, available at https://www.data.jma.go.jp/svd/eqev/data/bulletin/eqdoc_e.html (last accessed on 19 August 2020) and <http://www.hinet.bosai.go.jp/?LANG=en> (last accessed on 25 June 2020), and the moment tensor solutions by NIED F-net project (Fukuyama et al. 1998) available at <https://www.fnet.bosai.go.jp/top.php?LANG=en> (last accessed on 19 August 2020). The data analyses in this study were performed using PyTorch (Paszke et al. 2019), ObsPy (Beyreuther *et al.* 2010; Megies *et al.* 2011; Krischer *et al.* 2015), HASH (Hardebeck and Shearer 2002, 2008), and HASHpy (Williams 2014). I used Generic Mapping Tools (Wessel et al. 2013) for generating Figs. 3, 4, 5, 7, 10, 11, 12, and 13, and Matplotlib (Hunter 2007) for Figs. 2, 6, 8, and 9. This work was supported by Mitsubishi Foundation and AIST EDGE Runners project. In this work, the computation facility of the AI Bridging Cloud Infrastructure (ABCI) maintained by

367 AIST was employed.

368 References

- 369 Amante, C. & Eakins, B.W., 2009. ETOPO1 1 Arc-Minute Global Relief Model:
370 Procedures, Data Sources and Analysis. in *NOAA Technical Memorandum*
371 *NESDIS NGDC-24* National Geophysical Data Center, NOAA,
372 doi:10.7289/V5C8276M.
- 373 Beyreuther, M., Barsch, R., Krischer, L., Megies, T., Behr, Y. & Wassermann, J., 2010.
374 ObsPy: A Python Toolbox for Seismology, *Seismol. Res. Lett.*, 81, 530-533,
375 doi:10.1785/gssrl.81.3.530.
- 376 Brodsky, E.E., Saffer, D., Fulton, P., Chester, F., Conin, M., Huffman, K., Moore, J.C. &
377 Wu, H.-Y., 2017. The postearthquake stress state on the Tohoku megathrust as
378 constrained by reanalysis of the JFAST breakout data, *Geophys. Res. Lett.*, 44,
379 8294-8302, doi:10.1002/2017GL074027.
- 380 Chen, C. & Holland, A.A., 2016. PhasePAPy: A Robust Pure Python Package for
381 Automatic Identification of Seismic Phases, *Seismol. Res. Lett.*, 87, 1384-1396,
382 doi:10.1785/0220160019.
- 383 Dreger, D.S. & Helmberger, D.V., 1993. Determination of source parameters at regional
384 distances with three-component sparse network data, *J. Geophys. Res.*, 98,
385 8107-8125, doi:10.1029/93JB00023.
- 386 Ekström, G., Nettles, M. & Dziewoński, A.M., 2012. The global CMT project 2004–
387 2010: Centroid-moment tensors for 13,017 earthquakes, *Phys. Earth Planet. Inter.*,
388 200–201, 1-9, doi:10.1016/j.pepi.2012.04.002.
- 389 Fukuyama, E., Ishida, M., Dreger, D.S. & Kawai, H., 1998. Automated seismic moment

- 390 tensor determination by using on-line broadband seismic waveforms, *Zisin 2nd*
391 *Ser.*, 51, 149-156, doi:10.4294/zisin1948.51.1_149. (in Japanese with English
392 abstract)
- 393 Girshick, R., Donahue, J., Darrell, T. & Malik, J., 2014. Rich Feature Hierarchies for
394 Accurate Object Detection and Semantic Segmentation. in *2014 IEEE*
395 *Conference on Computer Vision and Pattern Recognition*, pp. 580-587,
396 doi:10.1109/CVPR.2014.81.
- 397 Hara, S., Fukahata, Y. & Iio, Y., 2019. P-wave first-motion polarity determination of
398 waveform data in western Japan using deep learning, *Earth Planets Space*, 71,
399 127, doi:10.1186/s40623-019-1111-x.
- 400 Hardebeck, J.L., 2015. Stress orientations in subduction zones and the strength of
401 subduction megathrust faults, *Science*, 349, 1213-1216,
402 doi:10.1126/science.aac5625.
- 403 Hardebeck, J.L. & Shearer, P.M., 2002. A new method for determining first-motion
404 focal mechanisms, *Bull. Seismol. Soc. Am.*, 92, 2264-2276,
405 doi:10.1785/0120010200.
- 406 Hardebeck, J.L. & Shearer, P.M., 2003. Using S/P amplitude ratios to constrain the focal
407 mechanisms of small earthquakes, *Bull. Seismol. Soc. Am.*, 93, 2434-2444,
408 doi:10.1785/0120020236.
- 409 Hardebeck, J.L. & Shearer, P.M., 2008. HASH: A FORTRAN program for computing
410 earthquake first-motion focal mechanisms – v1.2 –.
- 411 Heidbach, O., Rajabi, M., Cui, X., Fuchs, K., Müller, B., Reinecker, J., Reiter, K.,
412 Tingay, M., Wenzel, F., Xie, F., Ziegler, M.O., Zoback, M.-L. & Zoback, M.,
413 2018. The World Stress Map database release 2016: Crustal stress pattern across

- scales, *Tectonophysics*, 744, 484-498, doi:10.1016/j.tecto.2018.07.007.
- Heidbach, O., Rajabi, M., Reiter, K., Ziegler, M. & Team, W., 2016. World Stress Map Database Release 2016. in *GFZ Data Services*, doi:10.5880/WSM.2016.001.
- Heidbach, O., Tingay, M., Barth, A., Reinecker, J., Kurfeß, D. & Müller, B., 2008. The World Stress Map database release 2008, doi:10.1594/GFZ.WSM.Rel2008.
- Hornik, K., 1991. Approximation capabilities of multilayer feedforward networks, *Neural Networks*, 4, 251-257, doi:10.1016/0893-6080(91)90009-T.
- Huffman, K.A., Saffer, D.M. & Dugan, B., 2016. In situ stress magnitude and rock strength in the Nankai accretionary complex: a novel approach using paired constraints from downhole data in two wells, *Earth Planets Space*, 68, 123, doi:10.1186/s40623-016-0491-4.
- Hunter, J.D., 2007. Matplotlib: A 2D Graphics Environment, *Comput. Sci. Eng.*, 9, 90-95, doi:10.1109/MCSE.2007.55.
- Igarashi, T., 2020. Catalog of small repeating earthquakes for the Japanese Islands, *Earth Planets Space*, 72, 73, doi:10.1186/s40623-020-01205-2.
- Iio, Y., Kishimoto, S., Nakao, S., Miura, T., Yoneda, I., Sawada, M. & Katao, H., 2018. Extremely weak fault planes: An estimate of focal mechanisms from stationary seismic activity in the San'in district, Japan, *Tectonophysics*, 723, 136-148, doi:10.1016/j.tecto.2017.12.007.
- Imanishi, K., Ando, R. & Kuwahara, Y., 2012. Unusual shallow normal-faulting earthquake sequence in compressional northeast Japan activated after the 2011 off the Pacific coast of Tohoku earthquake, *Geophys. Res. Lett.*, 39, L09306, doi:10.1029/2012GL051491.
- Imanishi, K., Kuwahara, Y., Takeda, T., Mizuno, T., Ito, H., Ito, K., Wada, H. & Haryu,

- 438 Y., 2011. Depth-dependent stress field in and around the Atotsugawa fault,
439 central Japan, deduced from microearthquake focal mechanisms: Evidence for
440 localized aseismic deformation in the downward extension of the fault, *J.*
441 *Geophys. Res.*, 116, B01305, doi:10.1029/2010JB007900.
- 442 Imanishi, K., Uchide, T., Ohtani, M., Matsushita, R. & Nakai, M., 2019. Construction of
443 the crustal stress map in the Kanto region, central Japan, *Bull. Geol. Surv. Jpn.*,
444 70, 273-298. (in Japanese with English abstract)
- 445 Ioffe, S. & Szegedy, C., 2015. Batch normalization: accelerating deep network training
446 by reducing internal covariate shift. in *ArXiv e-prints*.
- 447 Kawanishi, R., Iio, Y., Yukutake, Y., Shibutani, T. & Katao, H., 2009. Local stress
448 concentration in the seismic belt along the Japan Sea coast inferred from precise
449 focal mechanisms: Implications for the stress accumulation process on intraplate
450 earthquake faults, *J. Geophys. Res. Solid Earth*, 114, doi:10.1029/2008jb005765.
- 451 Kingma, D.P. & Ba, J., 2014. Adam: A method for stochastic optimization, *arXiv*
452 *preprint arXiv:1412.6980*.
- 453 Krischer, L., Megies, T., Barsch, R., Beyreuther, M., Lecocq, T., Caudron, C. &
454 Wassermann, J., 2015. ObsPy: a bridge for seismology into the scientific Python
455 ecosystem, *Comput. Sci. Discov.*, 8, doi:10.1088/1749-4699/8/1/014003.
- 456 Ley, C. & Verdebout, T., 2017. *Modern directional statistics*, pp. 190, CRC Press, New
457 York, doi:10.1201/9781315119472.
- 458 Matsumoto, S., Nakao, S., Ohkura, T., Miyazaki, M., Shimizu, H., Abe, Y., Inoue, H.,
459 Nakamoto, M., Yoshikawa, S. & Yamashita, Y., 2015. Spatial heterogeneities in
460 tectonic stress in Kyushu, Japan and their relation to a major shear zone, *Earth*
461 *Planets Space*, 67, 172, doi:10.1186/s40623-015-0342-8.

- 462 Matsushita, R. & Imanishi, K., 2015. Stress fields in and around metropolitan Osaka,
463 Japan, deduced from microearthquake focal mechanisms, *Tectonophysics*, 642,
464 46-57, doi:10.1016/j.tecto.2014.12.011.
- 465 Megies, T., Beyreuther, M., Barsch, R., Krischer, L. & Wassermann, J., 2011. ObsPy –
466 What can it do for data centers and observatories?, *Ann. Geophys.*, 54, 12,
467 doi:10.4401/ag-4838.
- 468 Meneses-Gutierrez, A. & Nishimura, T., 2020. Inelastic deformation zone in the lower
469 crust for the San-in Shear Zone, Southwest Japan, as observed by a dense GNSS
470 network, *Earth Planets Space*, 72, 10, doi:10.1186/s40623-020-1138-z.
- 471 Nair, V. & Hinton, G.E., 2010. Rectified linear units improve restricted boltzmann
472 machines. in *27th International Conference on Machine Learning (ICML-10)*,
473 pp. 807-814, Haifa, Israel.
- 474 Nakamura, M., 2004. Automatic determination of focal mechanism solutions using
475 initial motion polarities of P and S waves, *Phys. Earth Planet. Inter.*, 146,
476 531-549, doi:10.1016/j.pepi.2004.05.009.
- 477 National Research Institute for Earth Science and Disaster Resilience, 2020. NIED
478 Hi-net, National Research Institute for Earth Science and Disaster Resilience.
479 doi:10.17598/NIED.0003.
- 480 Otsubo, M., Miyakawa, A. & Imanishi, K., 2018. Normal-faulting stress state associated
481 with low differential stress in an overriding plate in northeast Japan prior to the
482 2011 Mw 9.0 Tohoku earthquake, *Earth Planets Space*, 70,
483 doi:10.1186/s40623-018-0813-9.
- 484 Paszke, A., Gross, S., Massa, F., Lerer, A., Bradbury, J., Chanan, G., Killeen, T., Lin, Z.,
485 Gimelshein, N., Antiga, L., Desmaison, A., Kopf, A., Yang, E., DeVito, Z.,

- 486 Raison, M., Tejani, A., Chilamkurthy, S., Steiner, B., Fang, L., Bai, J. & Chintala,
487 S., 2019. PyTorch: An imperative style, high-performance deep learning library.
488 *in Advances in Neural Information Processing Systems*, pp. 8024-8035, Curran
489 Associates, Inc.
- 490 Pugh, D.J., White, R.S. & Christie, P.A.F., 2016a. Automatic Bayesian polarity
491 determination, *Geophys. J. Int.*, 206, 275-291, doi:10.1093/gji/ggw146.
- 492 Pugh, D.J., White, R.S. & Christie, P.A.F., 2016b. A Bayesian method for microseismic
493 source inversion, *Geophys. J. Int.*, doi:10.1093/gji/ggw186.
- 494 Ross, Z.E., Meier, M.-A. & Hauksson, E., 2018. P wave arrival picking and first-motion
495 polarity determination with deep learning, *J. Geophys. Res. Solid Earth*, 123,
496 5120-5129, doi:10.1029/2017JB015251.
- 497 Rumelhart, D.E., Hinton, G.E. & Williams, R.J., 1986. Learning representations by
498 back-propagating errors, *Nature*, 323, 533-536, doi:10.1038/323533a0.
- 499 Savage, M.K., Aoki, Y., Unglert, K., Ohkura, T., Umakoshi, K., Shimizu, H., Iguchi, M.,
500 Tameguri, T., Ohminato, T. & Mori, J., 2016. Stress, strain rate and anisotropy in
501 Kyushu, Japan, *Earth Planet. Sci. Lett.*, 439, 129-142,
502 doi:10.1016/j.epsl.2016.01.005.
- 503 Shearer, P.M., Prieto, G.A. & Hauksson, E., 2006. Comprehensive analysis of
504 earthquake source spectra in Southern California, *J. Geophys. Res.*, 111, B06303,
505 doi:10.1029/2005JB003979.
- 506 Srivastava, N., Hinton, G., Krizhevsky, A., Sutskever, I. & Salakhutdinov, R., 2014.
507 Dropout: a simple way to prevent neural networks from overfitting, *J. Mach.*
508 *Learn. Res.*, 15, 1929-1958.
- 509 Terakawa, T. & Matsu'ura, M., 2010. The 3-D tectonic stress fields in and around Japan

510 inverted from centroid moment tensor data of seismic events, *Tectonics*, 29,
 511 TC6008, doi:10.1029/2009TC002626.

512 Townend, J., Sutherland, R., Toy, V.G., Doan, M.-L., Célérrier, B., Massiot, C., Coussens,
 513 J., Jeppson, T., Janku-Capova, L., Remaud, L., Upton, P., Schmitt, D.R., Pezard,
 514 P., Williams, J., Allen, M.J., Baratin, L.-M., Barth, N., Becroft, L., Boese, C.M.,
 515 Boulton, C., Broderick, N., Carpenter, B., Chamberlain, C.J., Cooper, A., Coutts,
 516 A., Cox, S.C., Craw, L., Eccles, J.D., Faulkner, D., Grieve, J., Grochowski, J.,
 517 Gulley, A., Hartog, A., Henry, G., Howarth, J., Jacobs, K., Kato, N., Keys, S.,
 518 Kirilova, M., Kometani, Y., Langridge, R., Lin, W., Little, T., Lukacs, A.,
 519 Mallyon, D., Mariani, E., Mathewson, L., Melosh, B., Menzies, C., Moore, J.,
 520 Morales, L., Mori, H., Niemeijer, A., Nishikawa, O., Nitsch, O., Paris, J., Prior,
 521 D.J., Sauer, K., Savage, M.K., Schleicher, A., Shigematsu, N., Taylor-Offord, S.,
 522 Teagle, D., Tobin, H., Valdez, R., Weaver, K., Wiersberg, T. & Zimmer, M., 2017.
 523 Petrophysical, Geochemical, and Hydrological Evidence for Extensive
 524 Fracture-Mediated Fluid and Heat Transport in the Alpine Fault's Hanging-Wall
 525 Damage Zone, *Geochem. Geophys. Geosyst.*, 18, 4709-4732,
 526 doi:10.1002/2017GC007202.

527 Wessel, P., Smith, W.H.F., Scharroo, R., Luis, J. & Wobbe, F., 2013. Generic Mapping
 528 Tools: Improved Version Released, *EOS*, 94, 409-410,
 529 doi:10.1002/2013eo450001.

530 Williams, M.C., 2014. HASHpy, doi:10.5281/zenodo.9808.

531 Wu, H.-Y., Ma, K.-F., Zoback, M., Boness, N., Ito, H., Hung, J.-H. & Hickman, S., 2007.
 532 Stress orientations of Taiwan Chelungpu-Fault Drilling Project (TCDP) hole-A
 533 as observed from geophysical logs, *Geophys. Res. Lett.*, 34,

- 534 doi:10.1029/2006GL028050.
- 535 Yang, W., Hauksson, E. & Shearer, P.M., 2012. Computing a large refined catalog of
536 focal mechanisms for southern California (1981–2010): Temporal stability of the
537 style of faulting, *Bull. Seismol. Soc. Am.*, 102, 1179–1194,
538 doi:10.1785/0120110311.
- 539 Yoshida, K., Hasegawa, A. & Okada, T., 2015. Spatial variation of stress orientations in
540 NE Japan revealed by dense seismic observations, *Tectonophysics*, 647–648,
541 63–72, doi:10.1016/j.tecto.2015.02.013.
- 542 Yoshida, K., Hasegawa, A., Saito, T., Asano, Y., Tanaka, S., Sawazaki, K., Urata, Y. &
543 Fukuyama, E., 2016. Stress rotations due to the M6.5 foreshock and M7.3 main
544 shock in the 2016 Kumamoto, SW Japan, earthquake sequence, *Geophys. Res.*
545 *Lett.*, 43, 10097–10104, doi:10.1002/2016GL070581.
- 546

547 **Tables**

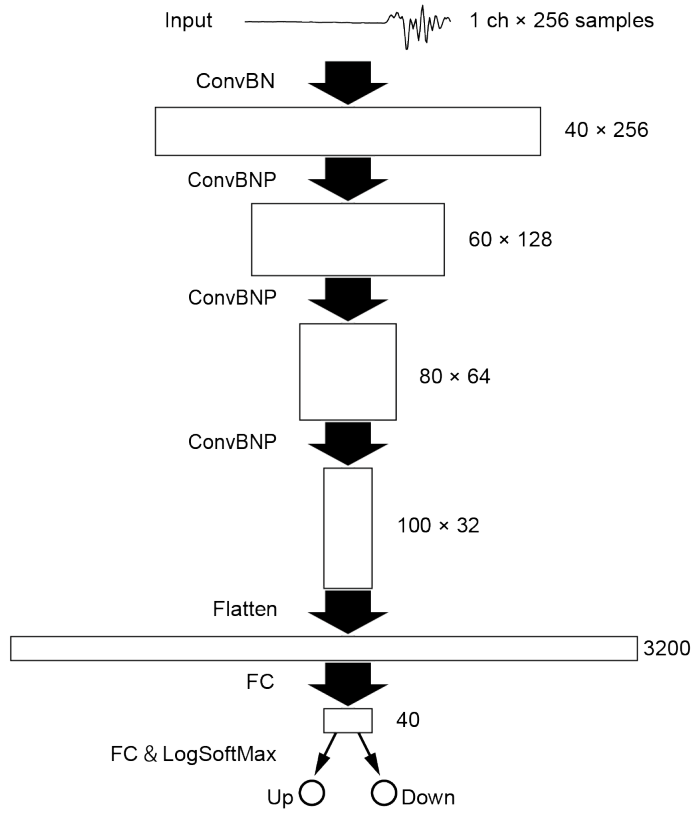
548 **Table 1**

549 Numbers of seismograms and earthquakes included in the data sets.

Region	Type of Data Set	Seismogram Sets	Earthquakes
Entire Japan	Training	404,989	18,721
	Validation	8,636	620
Kanto	Training	12,803	1,262
	Validation	782	56
	Test	1,483	113
Chugoku	Training	63,327	2,259
	Validation	7,672	322
	Test	12,818	595
Entire Japan	Application	2,301,584	114,525

550

Figures



552

553 Fig. 1

554 The design of the neural network model. The numbers on the right indicate the
 555 number of channels and samples, while “ConvBN,” “Conv BNP,” and “FC” denote
 556 convolution and batch normalization layers, convolution, batch normalization, and
 557 pooling layers, and fully connected layers, respectively.

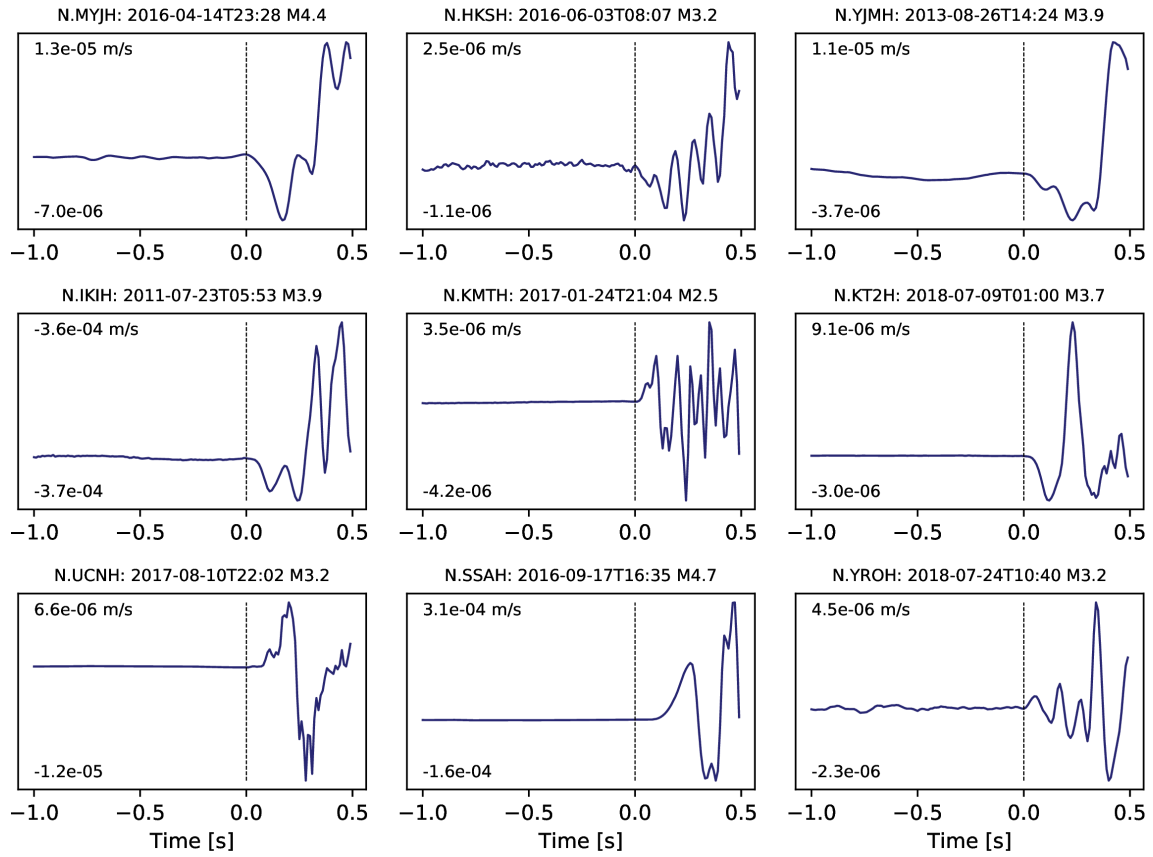


Fig. 2

Examples of seismograms with impulsive onsets but no accompanying polarity data in the JMA Unified Earthquake Catalog. Station names and the origin time and magnitude of the events are indicated above each panel. Note that this data was not used in the study.

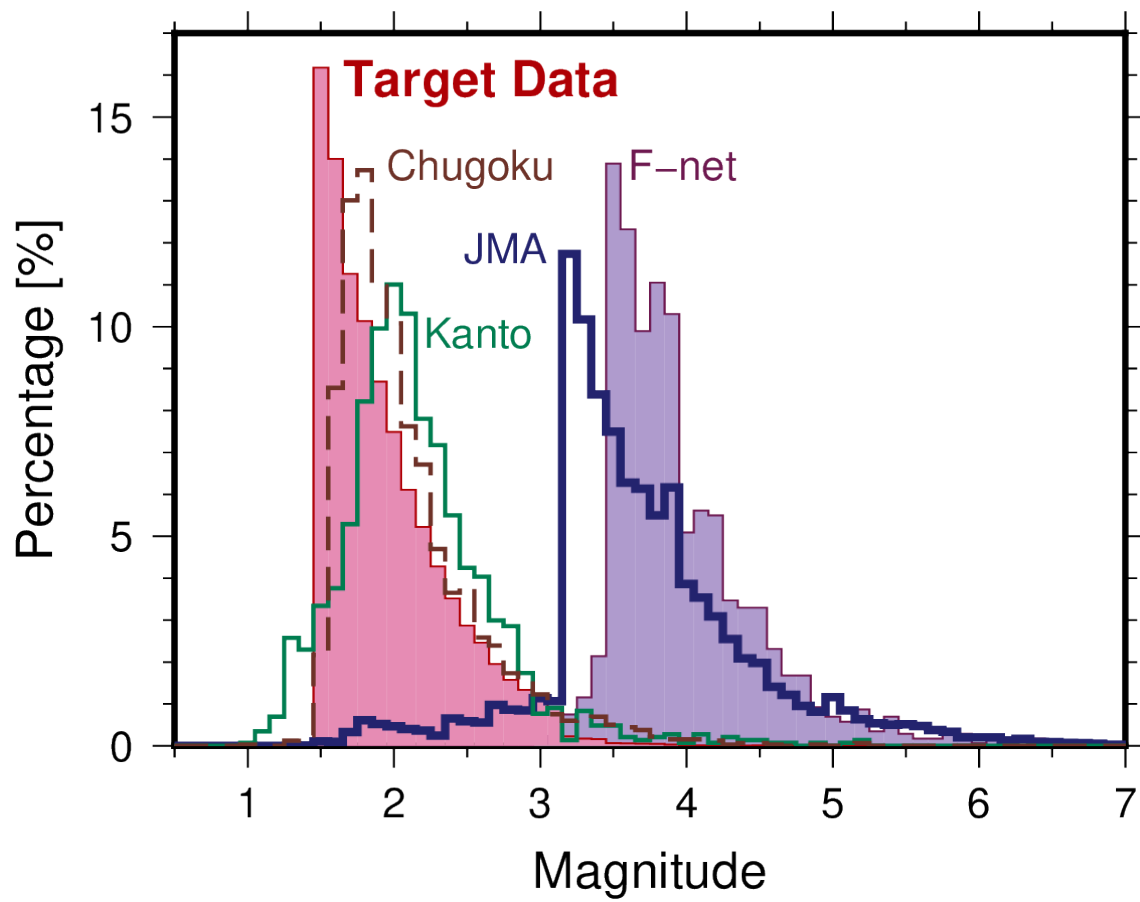


Fig. 3

Magnitude–frequency distributions in the data for the target (pink shade), F-net (purple shade), the JMA (thick navy), Kanto (thin green), and Chugoku (dashed brown) data sets.

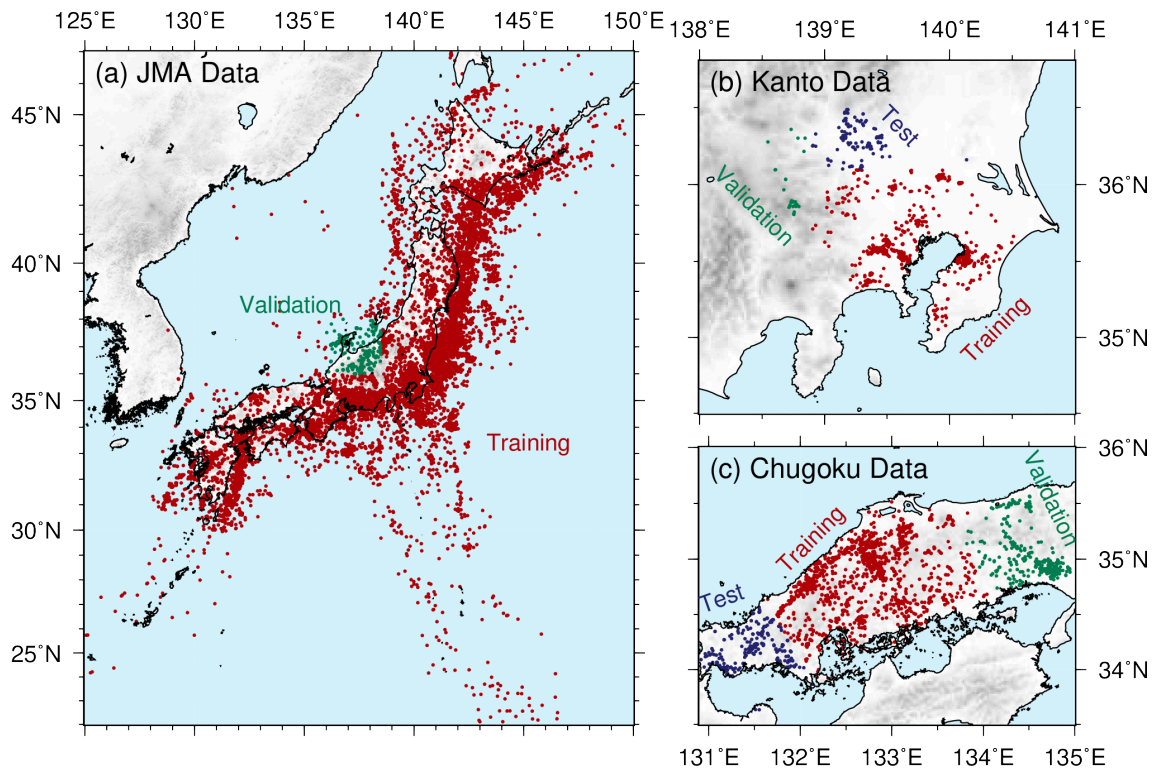
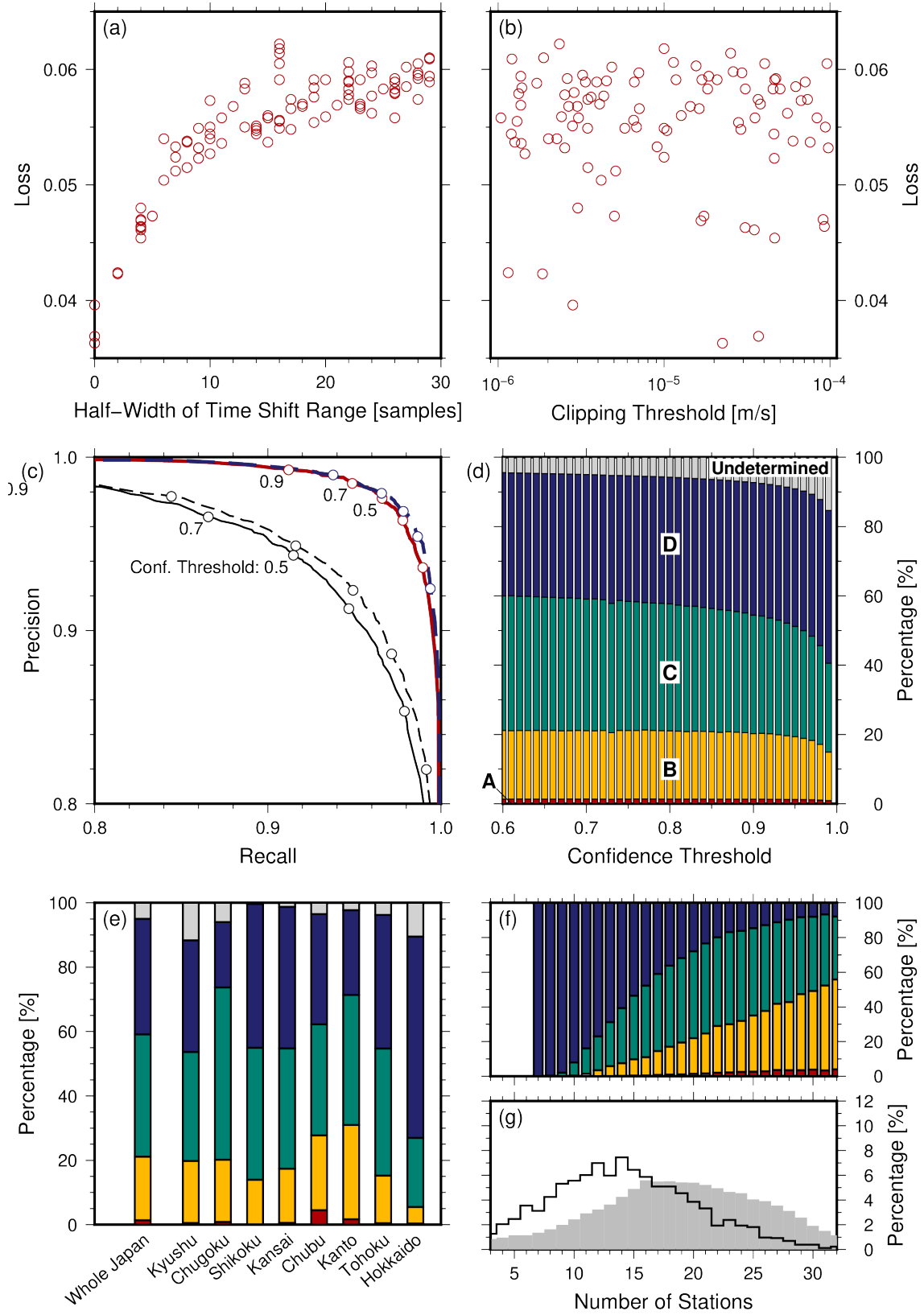


Fig. 4

Distribution of the epicentres of the earthquakes used for training (red), validation (green), and testing (blue) of the neural network model. The topography was taken from ETOPO1 (Amante and Eakins 2009).

574



575

Fig. 5

Summary of the results. Here, (a) and (b) show the loss function values as functions of the time-shift range and the clipping threshold, respectively. (c) The precision-recall curve of the trained model for the test data set. The thick red solid and blue dashed lines refer to the upward and downward polarities, respectively, in the case of the two-stage training. The thin black solid and dashed lines refer to the upward and downward polarities, respectively, where the model was trained using only the JMA data set. Circles correspond to every 0.1 units of the confidence thresholds. (d) Bar graphs of the rank of the focal mechanism solutions as a function of the confidence threshold. Red, yellow, green, and blue bars from the bottom to the top represent the A, B, C, and D-ranks, respectively. Gray bars on the top indicate undefined focal mechanisms. (e) Bar graphs of the rank of focal mechanism solutions for the whole of Japan and eight specific regions (see Fig. 7e). Here, a model with a confidence threshold of 0.7 was used. The color scheme is the same as in the case of (d). (f) Bar graphs as a function of the number of seismic stations. The color scheme is the same as for (d). (g) Histograms of events as a function of the number of stations. The black line and gray shaded region indicate the values for Hokkaido and other regions, respectively.

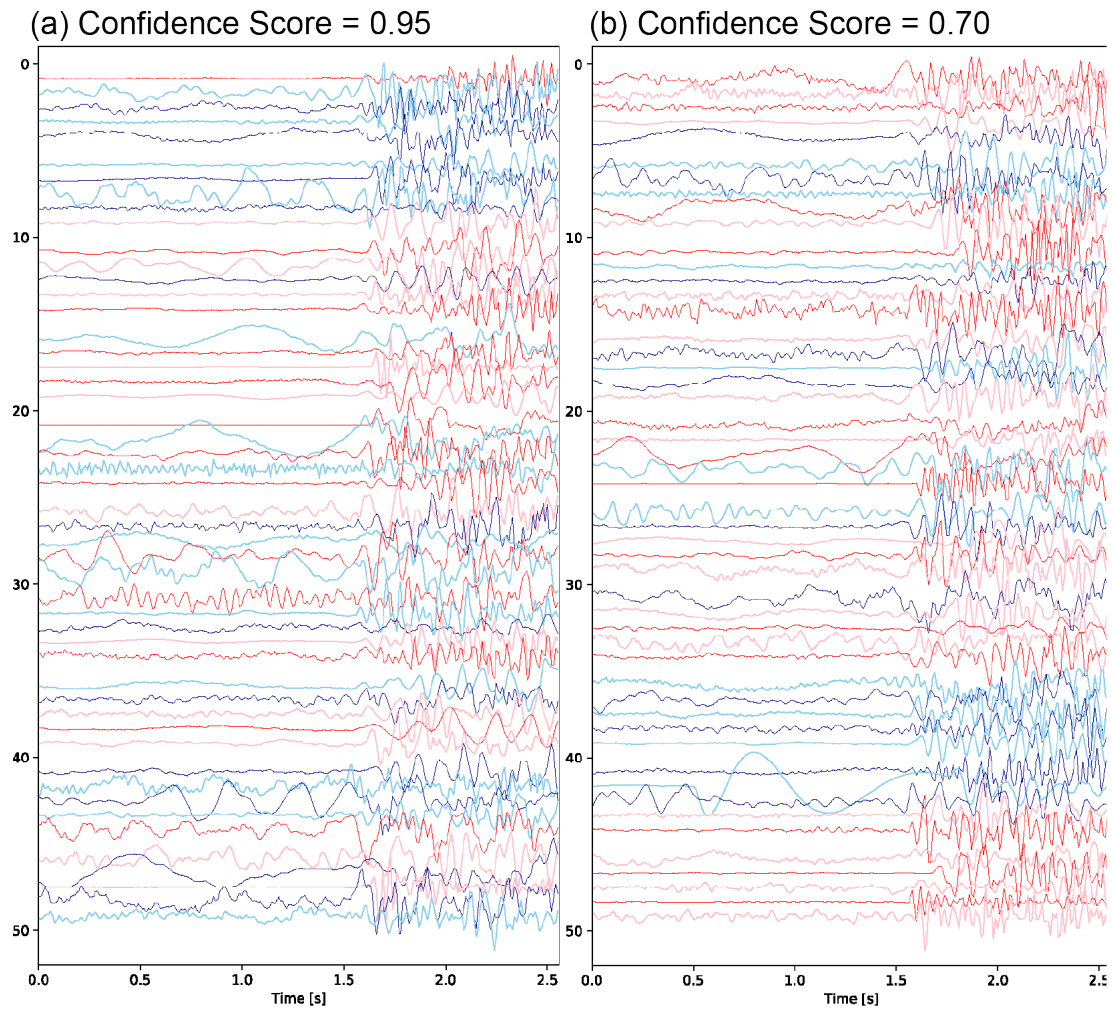


Fig. 6

Examples of seismograms with polarities picked by the neural network model with confidence scores of (a) 0.95 and (b) 0.70. Seismograms with downward polarities are flipped. If correctly picked, the first motion appears upward in this figure. Light and dark colors are alternated for convenience.

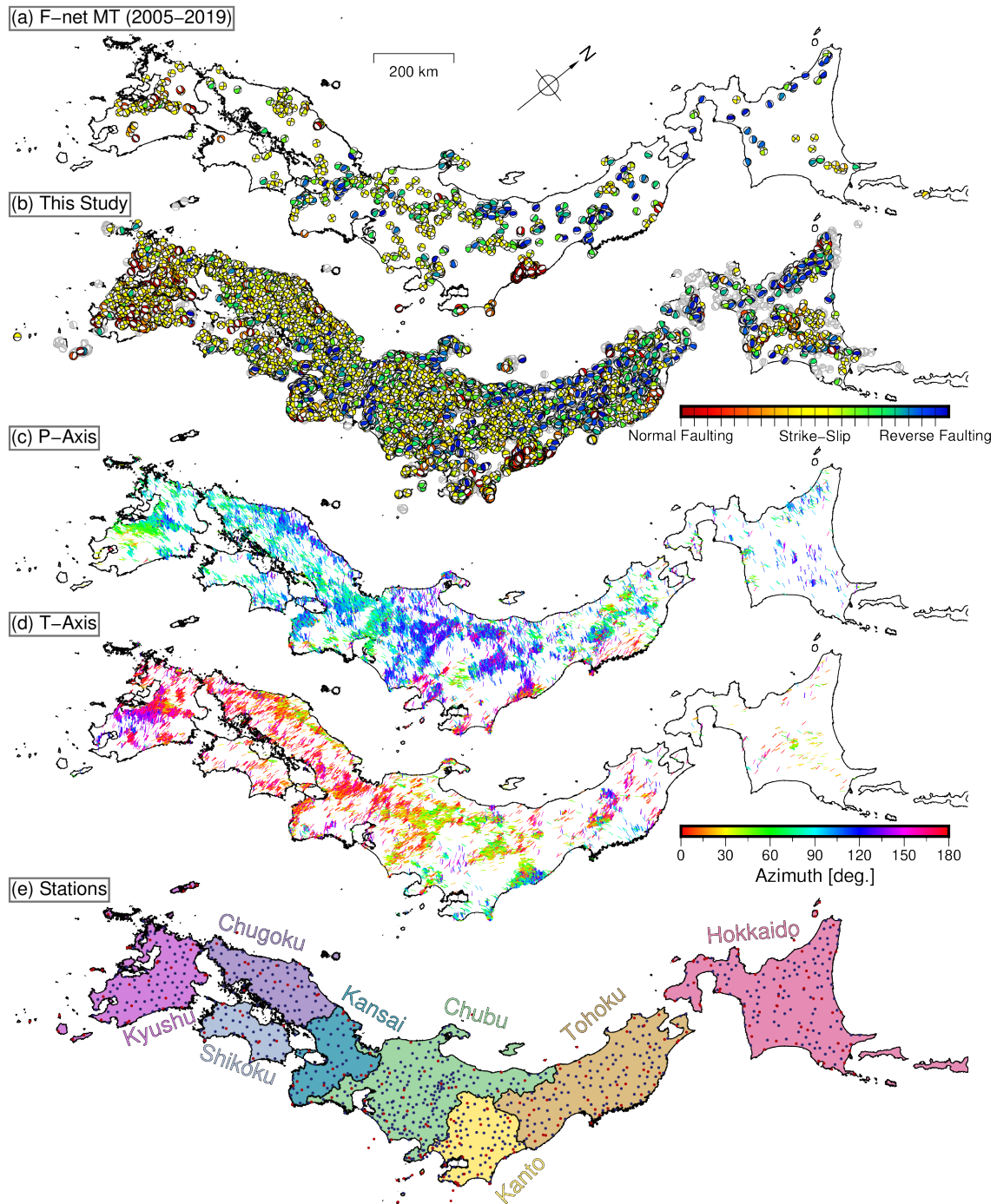


Fig. 7

(a) Moment tensor solutions of earthquakes from 2006–2019 provided by the NIED F-net project (Fukuyama et al. 1998) for reference. (b) Focal mechanism solutions derived by this study. Solutions ranked A–C (Hardebeck and Shearer 2008) are colored according to focal mechanism types (Shearer et al. 2006). The solutions ranked “D” is

605 shown by gray beach balls. (c) Azimuths of the P-axes of the estimated focal
606 mechanism solutions ranked A–C and with plunges less than 30° . Colors indicate the
607 azimuths. (d) Azimuths of the T-axes. (e) Seismic station distribution.

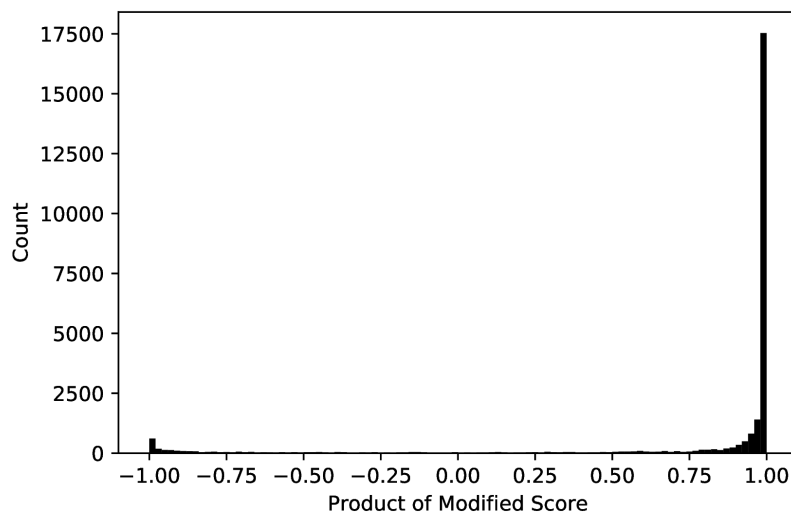


Fig. 8

Histogram of the product of the modified scores of repeating earthquake pairs, where the modified score is (confidence score for the upward polarity – that for the downward polarity).

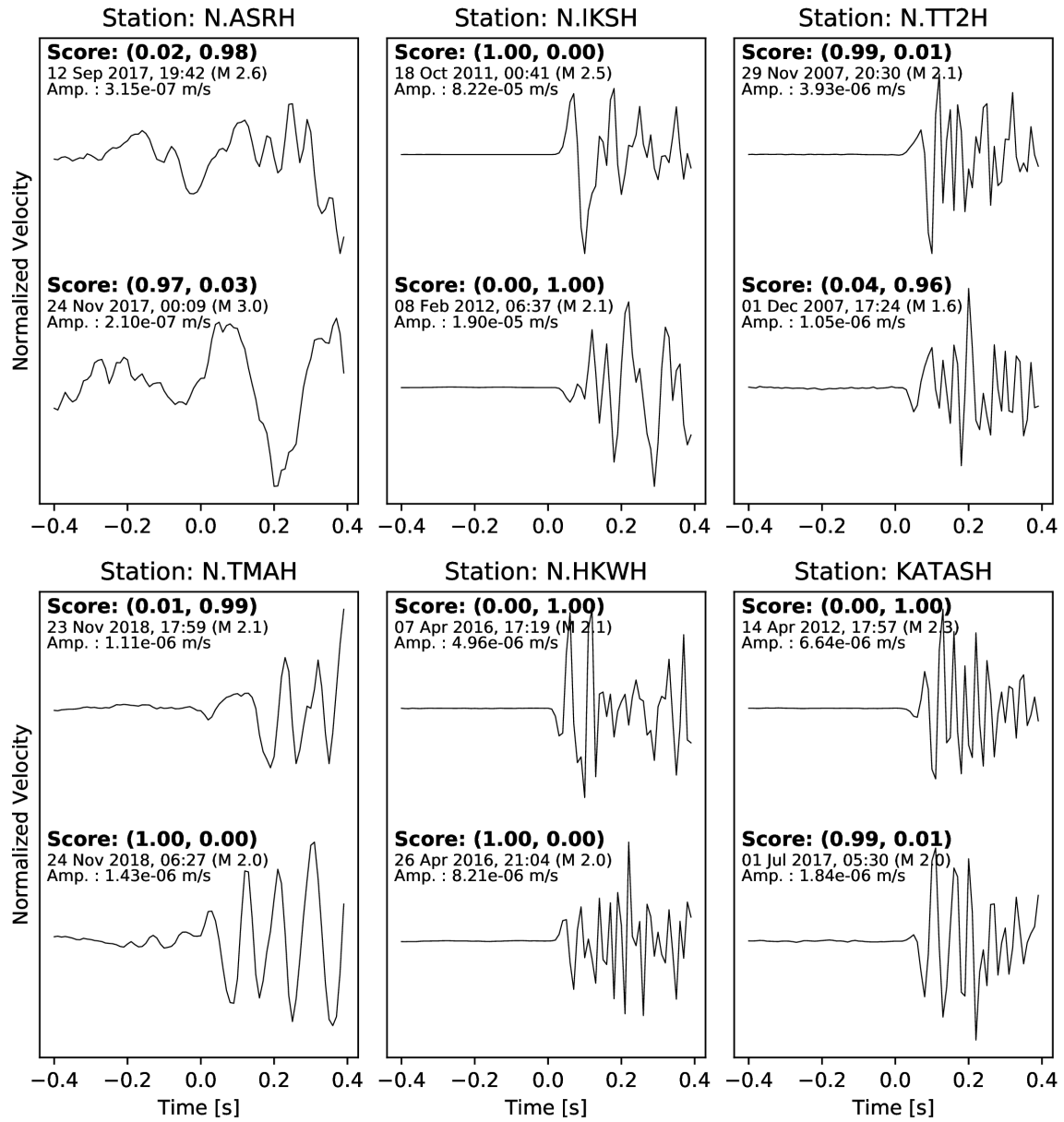
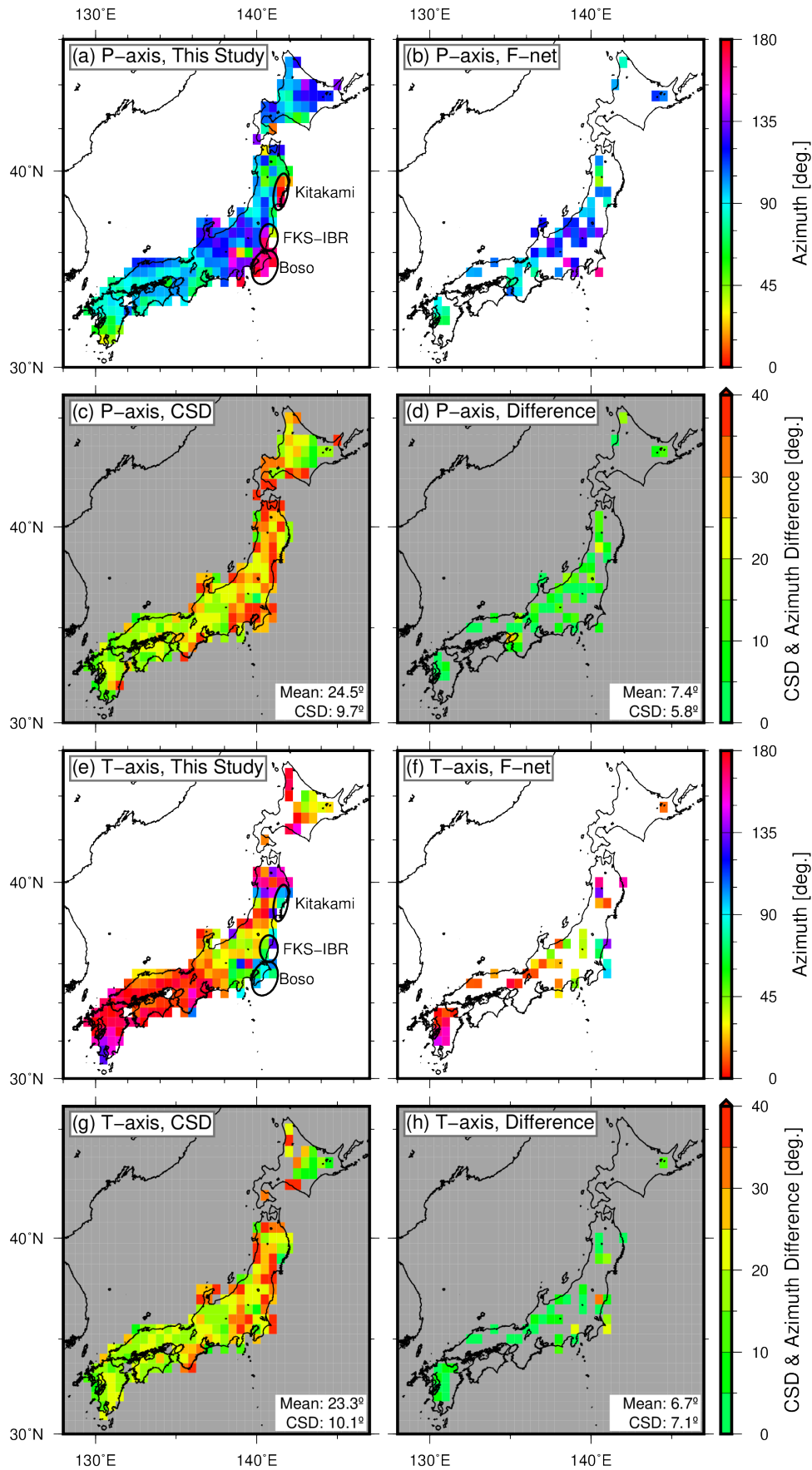


Fig. 9

Comparisons of seismograms of repeating earthquake pairs at the same stations. The scores shown in the panels are the confidence scores for the upward polarity.



618 Fig. 10

619 Spatial distributions of (a) the mean directions of P-axes azimuths from this study and
620 (b) the F-net catalog, (c) the circular standard deviation (CSD) (eq. (7)) of P-axes
621 azimuths from this study, and (d) the absolute values of differences of (a) and (b); (e)–
622 (h) are the values for T-axes. The P- or T- axes with lunge less than 30° and focal
623 mechanism solutions ranked A–C were used. The values at 0.5-degree grids with four or
624 more events are shown. In (a) and (e), the areas in the Kitakami mountain range,
625 Fukushima Hamadori and northern Ibaraki prefecture (FKS-IBR), and Boso peninsula
626 are marked by ellipses.

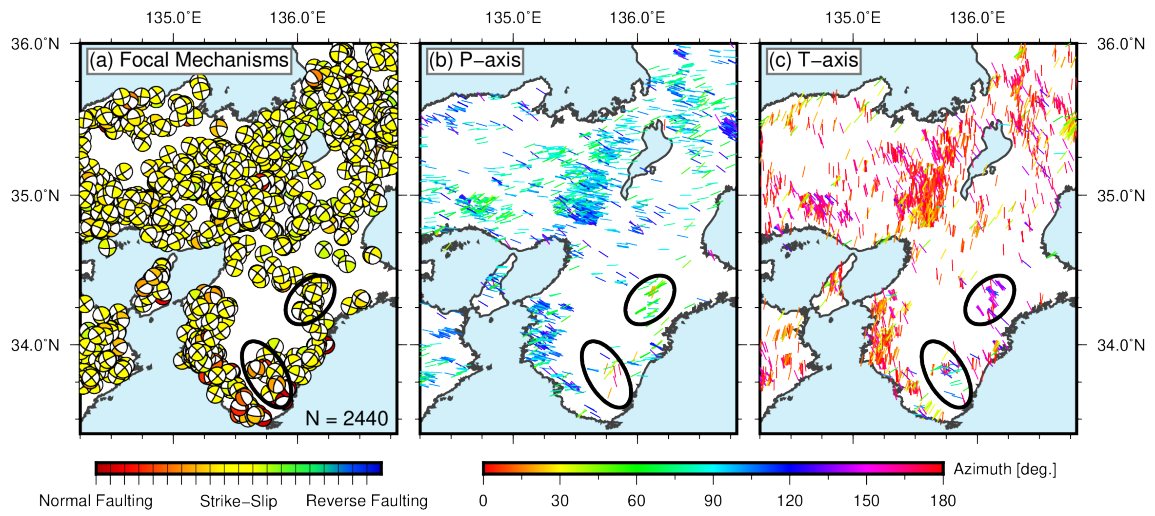


Fig. 11

(a) Focal mechanisms, (b) P-axes, and (c) T-axes in the Kansai area. In (b) and (c), the axes with plunges less than 30° and the focal mechanism solutions ranked A–C were plotted. The ellipses indicate areas with distinct focal mechanisms.

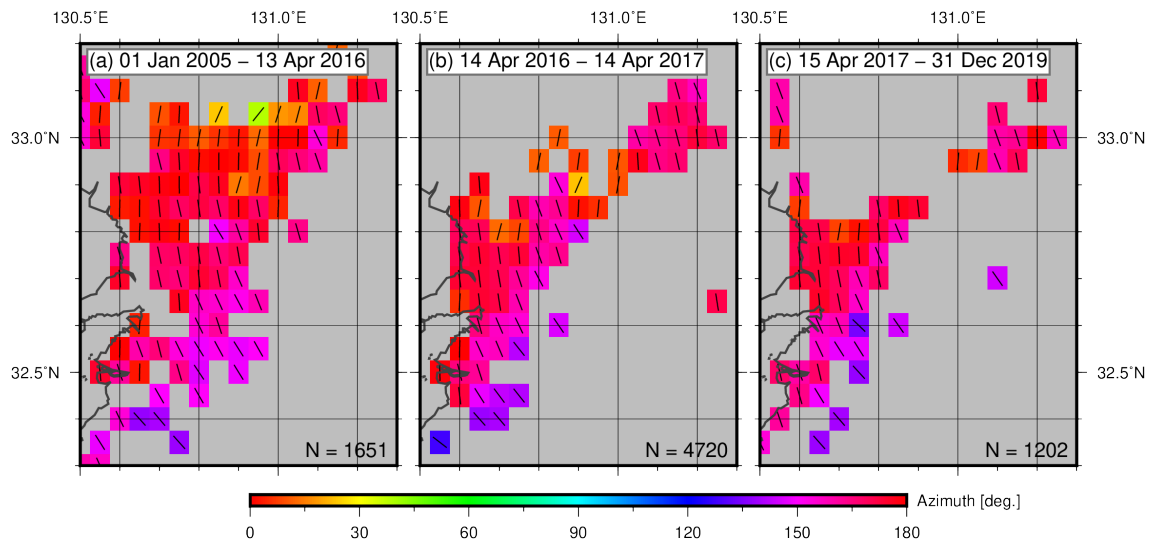


Fig. 12

The mean directions of the T-axes azimuths at 0.05-degree grids (a) before the 2016 Kumamoto earthquake, (b) within one year of the Kumamoto earthquake, and (c) after this time, indicated by short bars and colors. T-axes with plunges less than 30° and the focal mechanism solutions ranked A–C were used.

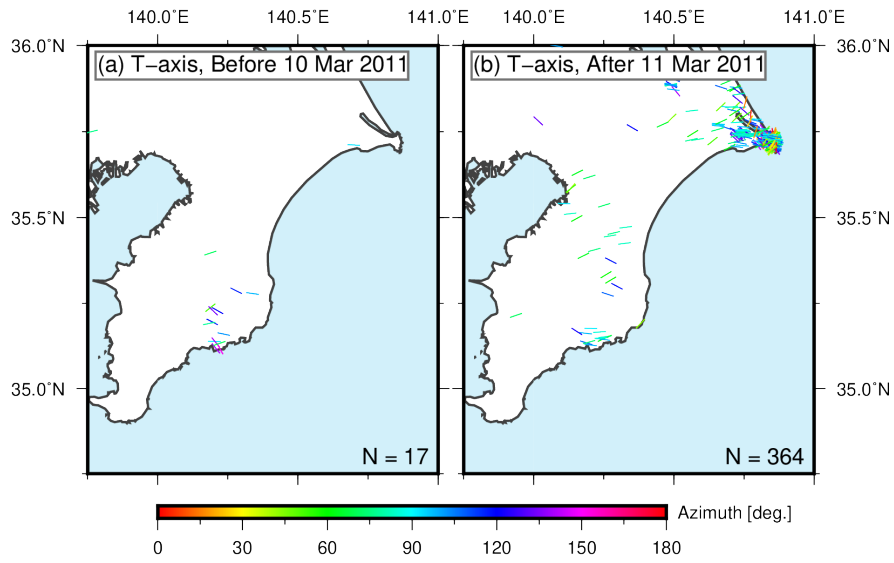


Fig. 13

The T-axis azimuths in the Boso peninsula (a) before and (b) after the 2011 Tohoku-oki earthquake. T-axes with plunges less than 30° and the focal mechanism solutions ranked A–C were plotted.